

Application of the generalized vector sampled pattern matching method to reconstruction of electrical capacitance CT images

Masahiro Takei¹ and Yoshifuru Saito²

¹ Department of Mechanical Engineering, Nihon University, 1-8-14 Kanda Surugadai Chiyoda Tokyo 101-8308, Japan

² Department of Art and Technology, Hosei University, Tokyo, Japan

E-mail: takei@mech.cst.nihon-u.ac.jp

Received 14 December 2003

Published 16 June 2004

Online at stacks.iop.org/MST/15/1371

doi:10.1088/0957-0233/15/7/021

Abstract

A new reconstruction method called generalized vector sampled pattern matching (GVSPM) has been applied to an ill-posed inverse problem involving electrical capacitance computed tomography for solid–air two-phase flow. This new method is able to achieve stable convergence without the use of an empirical value. This accurate reconstruction is accomplished using an objective function that is calculated as the inner product calculation between the experimental capacitance and the reconstructed image capacitance. The GVSPM method is compared with the conventional Landweber (LW) and iterative Tikhonov regularization (ITR) methods in terms of capacitance residual, image error and image correlation. Overall, the accuracy is strongly dependent upon the image type and the iteration number, however the GVSPM method proved superior to the LW and the ITR methods in the case of annular pseudo particle images.

Keywords: ECT, image reconstruction, GVSPM, ill-posed inverse problem

(Some figures in this article are in colour only in the electronic version)

List of symbols

C	$n \times 1$ measured capacitance column vector	N_y	y axial space resolution (=32)
$C_{i,j}$	measured capacitance between a standard electrode i and a reference electrode j	\mathbf{r}	position vector on the cross section, $\mathbf{r} = (x, y)$
C_R	capacitances residual	\mathbf{S}_e	$n \times m$ sensitivity map matrix normalized with the row elements' maximum value
DCR	dispersion concentration rate for simulation	\mathbf{T}	state transition matrix in equation (23)
\mathbf{E}	$m \times 1$ permittivity distribution column vector (=particle concentration distribution)	$V_i(\mathbf{r})$	potential distribution on a cross section between the i th and j th electrodes
I	iteration number	\mathbf{I}_m	$m \times m$ unit matrix
I_C	image capacitance	\mathbf{O}	$n \times 1$ zero column vector
I_E	image error	α	gain value of Landweber method in equation (16)
m	spatial resolution, $m = 32 \times 32 = 1024$	β	area ratio of one pixel to the whole pipe cross section
n	total number of electrode pairs, $n = 66$	γ	empirical value of iterative Tikhonov regularization in equation (17)
N_x	x axial space resolution (=32)		

$\varepsilon(\mathbf{r})$ relative permittivity distribution on a cross section
 λ eigenvalue in equation (24)

Superscripts

' normalization with norm
 * normalization with minimum value 0.0 and maximum value 1.0
 exp experimental data
 ini initial number
 k iteration number
 T transpose matrix

Font Type

Italic scalar or element in matrix
Bold matrix or column vector
Bold Italic row vector

1. Introduction

The use of non-invasive monitoring, such as computed tomography (CT), in multiphase flow measurement has recently become increasingly popular. The electrical capacitance CT has been investigated as a visualization technique for the solid behaviour in solid–air two-phase flow (Huang *et al* 1989, Halow and Nicoletti 1992, Dyakowski *et al* 1999). In capacitance CT, a sensor containing several electrodes is wrapped around the circumference of a pipeline, and the capacitances between the electrodes are measured. The particle concentration distribution, which is based on the permittivity distribution in a cross section, is obtained from the experimental capacitances. This is performed using an image reconstruction technique that is based on an ill-posed mathematical inverse problem. Because inverse problems are heavily dependent upon the system equation, a suitable image reconstruction technique for this capacitance CT is necessary. A variety of image reconstruction techniques have already been proposed (Isaksen 1996). Recently, iterative techniques such as the Landweber (LW) method and the iterative Tikhonov regularization (ITR) method have been widely used because of the relatively high accuracy of their reconstruction images (Yang and Peng 2003). These conventional reconstruction techniques, however, have several drawbacks with regard to empirical value setting and convergence at an infinite number of iterations. For example, the Landweber method requires an empirical gain value in order to converge upon the image, and it strongly depends upon the iteration number. It indicates that an image that has been processed over a suitable number of iterations will become extremely distorted (Liu *et al* 2001). Therefore, the Landweber method requires advance knowledge of the empirical gain value and the empirical iteration number. The iterative Tikhonov regularization method, on the other hand, needs an empirical value to use the singular value decomposition of the system equation to produce a pseudo inverse matrix. These conventional reconstruction methods are not able to accurately reconstruct an image with empirical values because they do not use an objective function to confirm the stability of the solution during the iterative process.

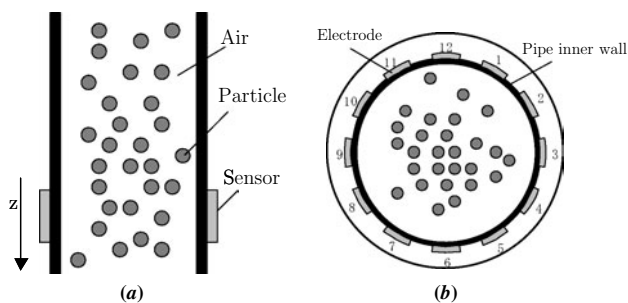


Figure 1. Overview of capacitance tomography. (a) Frontal view and (b) Cross sectional view.

In order to overcome the drawbacks of these iterative methods, Saito proposed a novel solution strategy called the sampled pattern matching (SPM) method for ill-posed linear inverse problems (Saito *et al* 1990). This inverse problem solver was then generalized for various types of linear system equations. The generalized solver, called generalized vector sampled pattern matching (GVSPM), has already been applied to the optimization of electron beam dosing (Saotome *et al* 1995, Yoda *et al* 1997). The key idea of GVSPM lies in an objective function that estimates convergence from the angle obtained by the inner product between the input vector and the solution vector. However, the GVSPM method has not yet been used as a reconstruction technique for the electrical capacitance CT.

In this study, the new GVSPM method is applied to the reconstruction of particle distribution images. This paper details the characteristics of this method that were examined using a simulation for pseudo particle concentration distribution images. The results of this simulation were then compared to those from the conventional Landweber and iterative Tikhonov regularization methods. The results in three areas were compared: capacitance residual, image error and image correlation.

2. Governing matrix equation for capacitance CT

The capacitance CT sensor is shown in figures 1(a) and (b). The 12 sensor electrodes are separated by insulation materials (Yang 1996). The relationship between capacitance and permittivity in a static-electro field is expressed by

$$C_{i,j} = -\frac{\varepsilon_0}{V_c} \oint_{r \in \Gamma_j} \varepsilon(\mathbf{r}) \nabla V_i(\mathbf{r}) \cdot d\mathbf{r} \quad (1)$$

where i is the standard electrode number that ranges from 1 to 11, and j is the reference electrode number, which ranges from $i + 1$ to 12. $C_{i,j}$ is the measured capacitance between the standard electrode i and the reference electrode j , ε_0 is the known vacuum permittivity, $\varepsilon(\mathbf{r})$ is the relative permittivity distribution on the cross section, \mathbf{r} is a position vector on the cross section: $\mathbf{r} = (x, y)$, V_c is the known voltage to the i th electrode, Γ_j is the area affected by the electric line of force and $V_i(\mathbf{r})$ is the potential distribution on the cross section between the i th and j th electrodes. Even though the values of $\varepsilon(\mathbf{r})$ and $V_i(\mathbf{r})$ in equation (1) are unknown, $\varepsilon(\mathbf{r})$ can be approximated by assuming that the electric charge's linear coupling at a position \mathbf{r} with a weight of sensitivity in Γ_j area is the total capacitance. As detailed in a previous work (Williams and

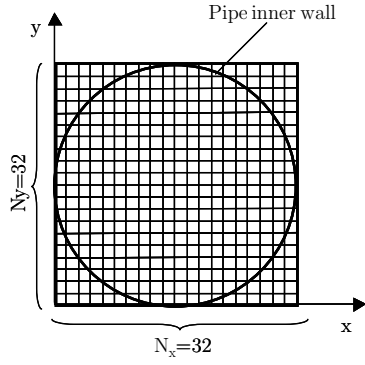


Figure 2. Space resolution.

Beck 1995, Polydorides and Lionheart 2002), when a particle exists solely in an infinitely small $\Delta x \times \Delta y$ area at the centre point $\mathbf{r} = \mathbf{r}_0$ between the i and j electrodes, and air exists at the remaining positions, the Laplace equation

$$\nabla \cdot [\varepsilon(\mathbf{r}_0) \nabla V(\mathbf{r}_0)] = 0 \quad (2)$$

is assumed to hold in the cross section. A finite element method can be used to discretize equation (2), and the distribution of $V_i(\mathbf{r})$ can be obtained by substituting the boundary conditions into equation (1). Next, the capacitance value $C_{i,j}^{r_0}$ with a particle at $\mathbf{r} = \mathbf{r}_0$ is obtained. The sensitivity value for a particle at $\mathbf{r} = \mathbf{r}_0$ is calculated using

$$S_{i,j}^{r_0} = \left(\frac{1}{\beta} \right) \frac{C_{i,j}^{r_0} - C_{i,j}^{\text{air}}}{C_{i,j}^{\text{particle}} - C_{i,j}^{\text{air}}} \quad \beta = \left(\frac{D^2}{N_x N_y} \right) / \pi \left(\frac{D}{2} \right)^2 \quad (3)$$

where $C_{i,j}^{\text{air}}$ and $C_{i,j}^{\text{particle}}$ are the capacitances when particles and air occupy the pipe cross section, respectively. The coefficient β represents the area ratio of one pixel to the entire pipe cross section, D is the diameter of the pipe, and N_x and N_y are x and y axial spatial resolutions, as depicted in figure 2. The sensitivity values are repeatedly obtained from equations (2) and (3) at every position and for all electrode pairs from 1–2 to 1–7, considering the symmetrical structure. Finally, $C_{i,j}$ is expressed as the linear coupling of $\varepsilon(\mathbf{r})$ with weight $S_{i,j}^r$ under an assumption of small spatial perturbations of $\varepsilon(\mathbf{r})$, that is

$$C_{i,j} = \sum_{\mathbf{r}=(1,1)}^{(N_x, N_y)} S_{i,j}^r \varepsilon(\mathbf{r}). \quad (4)$$

Equation (4) can be rewritten as the following matrix

expression:

$$\mathbf{C} = \mathbf{S}_e \mathbf{E}. \quad (5)$$

In other words, the capacitance \mathbf{C} can be used to obtain the permittivity distribution of particles \mathbf{E} in the cross section from both the known sensitivity map matrix \mathbf{S}_e and the measured capacitance matrix \mathbf{C} . In the case of 12 electrodes and $32 \times 32 = 1024$ pixels in the pipe cross section, as in figure 2, the sensitivity matrix \mathbf{S}_e in equation (5) is a 66×1024 matrix, the capacitance matrix \mathbf{C} is a 66×1 column vector, and the permittivity distribution matrix \mathbf{E} is a 1024×1 column vector. The mathematical method used to obtain the permittivity matrix \mathbf{E} from both the capacitance matrix \mathbf{C} and the sensitivity matrix \mathbf{S}_e is an ill-posed inverse problem because the inverse matrix \mathbf{S}_e^{-1} does not exist. The raw values of \mathbf{S}_e have an extremely wide range; the sensitivity to an adjacent electrode pair is more than 100 times larger than that to an opposing electrode pair. Figure 3 shows the two-dimensional distribution revised in the first through sixth rows of the sensitivity matrix \mathbf{S}_e . The white colour represents high values and the black colour represents low values.

3. GVSPM method theory for inverse problem

3.1. GVSPM objective function

Although the generalized vector sampled pattern matching method is an iterative method, it has one characteristic that other iterative methods do not have: the inclusion of an objective function in the general solution (Endo *et al* 2002). As a result, the GVSPM method is able to converge upon a reconstructed particle concentration image stably without setting a gain value. The objective function of the k th iterative particle distribution $\mathbf{E}^{(k)}$, $\mathbf{f}(\mathbf{E}^{(k)})$, is given by

$$\mathbf{f}(\mathbf{E}^{(k)}) = \mathbf{C}'^{(\text{exp})} \cdot \mathbf{C}'^{(k)} \rightarrow 1.0. \quad (6)$$

This objective function uses an inner product to determine whether the solution converges between the capacitance of k th iterative particle concentration image, $\mathbf{C}'^{(k)}$, and the experimental capacitance, $\mathbf{C}'^{(\text{exp})}$. Here, the prime symbol ' indicates normalization by the norm, that is

$$\mathbf{C}' = \frac{\mathbf{C}}{|\mathbf{C}|}.$$

In this equation, $|\cdot|$ indicates the norm. For instance, the norm of \mathbf{C} is the square root of the square sum of each element

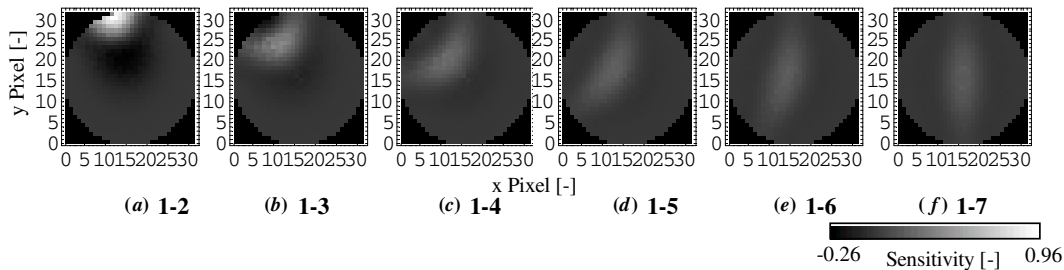


Figure 3. Sensitivity map matrices. (Standard electrode: 1, reference electrodes: 2–7.)

$$|\mathbf{C}| = \sqrt{c_1^2 + c_2^2 + \dots + c_n^2}. \quad (7)$$

The lower case c is an element of \mathbf{C} , and n is the total number of the electrode pairs, $n = 66$. The particle concentration distribution obtained by GVSPM method is $\mathbf{E}^{(k)}$ when $\mathbf{f}(\mathbf{E}^{(k)})$ approaches 1.0.

3.2. Iterative solution by the GVSPM method

From equation (5), the capacitance matrix \mathbf{C} can be expressed using the i th column vector of \mathbf{S}_e , \mathbf{S}_{ei} , and the i th element of \mathbf{E} , e_i , as

$$\mathbf{C} = \mathbf{S}_e \mathbf{E} = \sum_{i=1}^m (\mathbf{S}_{ei} e_i) \quad (8)$$

where m is the spatial resolution, $m = 1024$. Equation (8) normalized by the norm results in

$$\frac{\mathbf{C}}{|\mathbf{C}|} = \sum_{i=1}^m \left(\frac{\mathbf{S}_{ei}}{|\mathbf{S}_{ei}|} \frac{e_i}{|\mathbf{C}| / |\mathbf{S}_{ei}|} \right) \quad (9)$$

$$\mathbf{C}' = \sum_{i=1}^m (\mathbf{S}'_{ei} e'_i) = \mathbf{S}'_e \mathbf{E}'$$

where \mathbf{C} and \mathbf{S}_e are normalized by their norms. However, \mathbf{E} is not normalized by itself. The initial capacitance obtained from the experiment $\mathbf{C}^{(\text{exp})}$ and the initial value of \mathbf{E} given by the linear back projection method $\mathbf{E}^{(\text{ini})}$ can be combined in equation (9) to calculate the normalized $\mathbf{E}^{(\text{ini})}$

$$\mathbf{E}'^{(1)} \approx \mathbf{S}'_e{}^T \mathbf{C}'^{(\text{exp})}. \quad (10)$$

Here, $\mathbf{S}'_e{}^T$ is the transpose matrix of \mathbf{S}'_e . $\mathbf{E}'^{(\text{ini})}$ is an approximate particle concentration distribution because $\mathbf{S}'_e{}^T \mathbf{S}'_e$ is not a unit matrix. Substituting the value for $\mathbf{E}'^{(\text{ini})}$ in equation (10) for the \mathbf{E}' in equation (9) results in the norm-normalized $\mathbf{C}'^{(1)}$:

$$\mathbf{C}'^{(1)} = \frac{\mathbf{S}'_e \mathbf{E}'^{(\text{ini})}}{|\mathbf{S}'_e \mathbf{E}'^{(\text{ini})}|}. \quad (11)$$

The capacitance difference between $\mathbf{C}'^{(\text{exp})}$ and $\mathbf{C}'^{(1)}$, $\Delta \mathbf{C}'^{(1)}$, and the approximate value of the permittivity difference are

$$\Delta \mathbf{C}'^{(1)} = \mathbf{C}'^{(1)} - \mathbf{C}'^{(\text{exp})} \quad (12)$$

$$\Delta \mathbf{E}'^{(1)} \approx \mathbf{S}'_e{}^T \Delta \mathbf{C}'^{(1)}. \quad (13)$$

The first iterative permittivity value $\mathbf{E}'^{(1)}$ is obtained by subtracting equation (13) from the initial permittivity value $\mathbf{E}'^{(\text{ini})}$

$$\begin{aligned} \mathbf{E}'^{(1)} &= \mathbf{E}'^{(\text{ini})} - \Delta \mathbf{E}'^{(1)} = \mathbf{E}'^{(\text{ini})} - \mathbf{S}'_e{}^T \Delta \mathbf{C}'^{(1)} \\ &= \mathbf{E}'^{(\text{ini})} - \mathbf{S}'_e{}^T \left(\frac{\mathbf{S}'_e \mathbf{E}'^{(\text{ini})}}{|\mathbf{S}'_e \mathbf{E}'^{(\text{ini})}|} - \mathbf{C}'^{(\text{exp})} \right). \end{aligned} \quad (14)$$

Based on equation (14) the relationship between the k th iterative solution, $\mathbf{E}'^{(k)}$, and the $(k-1)$ th iterative solution, $\mathbf{E}'^{(k-1)}$, is

$$\begin{aligned} \mathbf{E}'^{(k)} &= \mathbf{E}'^{(k-1)} - \mathbf{S}'_e{}^T \Delta \mathbf{C}'^{(k-1)} \\ &= \mathbf{E}'^{(k-1)} - \mathbf{S}'_e{}^T \left(\frac{\mathbf{S}'_e \mathbf{E}'^{(k-1)}}{|\mathbf{S}'_e \mathbf{E}'^{(k-1)}|} - \mathbf{C}'^{(\text{exp})} \right). \end{aligned} \quad (15)$$

The Landweber and the iterative Tikhonov regularization methods are provided below as a reference (Yang and Peng 2003).

The Landweber iterative method is

$$\begin{aligned} \mathbf{E}^{*(k)} &= \mathbf{E}^{*(k-1)} - \alpha \mathbf{S}'_e{}^T \Delta \mathbf{C}^{*(k-1)} \\ &= \mathbf{E}^{*(k-1)} - \alpha \mathbf{S}'_e{}^T (\mathbf{S}_e \mathbf{E}^{*(k-1)} - \mathbf{C}^{*(\text{exp})}). \end{aligned} \quad (16)$$

The iterative Tikhonov regularization is

$$\begin{aligned} \mathbf{E}^{*(k)} &= \mathbf{E}^{*(k-1)} \\ &\quad - (\mathbf{S}'_e{}^T \mathbf{S}_e + \gamma \mathbf{I})^{-1} \mathbf{S}'_e{}^T (\mathbf{S}_e \mathbf{E}^{*(k-1)} - \mathbf{C}^{*(\text{exp})}). \end{aligned} \quad (17)$$

In these equations, \mathbf{C}^* is a normalization using a minimum value of 0.0 and a maximum value of 1.0 at every iteration, which is similar to the GVSPM method. \mathbf{E}^* , though, is not normalization by itself. The Landweber and the iterative Tikhonov regularization methods need empirical values α and γ , however, the GVSPM method does not need an empirical value.

3.3. Inclusion of objective function in iterative solution

The distinguishing characteristic of GVSPM is that it includes an objective function in the iterative solution. Equations (6) through (11) result in

$$1.0 - \mathbf{f}(\mathbf{E}^{(k)}) = 1.0 - \mathbf{C}'^{(\text{exp})} \cdot \left[\frac{\mathbf{S}'_e \mathbf{E}'^{(k-1)}}{|\mathbf{S}'_e \mathbf{E}'^{(k-1)}|} \right]^T \rightarrow 0.0. \quad (18)$$

Because $\mathbf{S}'_e \mathbf{E}'^{(k-1)} / |\mathbf{S}'_e \mathbf{E}'^{(k-1)}|$ is a column vector $\mathbf{C}'^{(k)}$, a transpose operation is needed to convert it to a row vector. Multiplying equation (18) by the row vector $\mathbf{C}'^{(\text{exp})}$ obtains

$$\mathbf{C}'^{(\text{exp})} - \mathbf{C}'^{(\text{exp})} \cdot \mathbf{C}'^{(\text{exp})} \left[\frac{\mathbf{S}'_e \mathbf{E}'^{(k-1)}}{|\mathbf{S}'_e \mathbf{E}'^{(k-1)}|} \right]^T \rightarrow \mathbf{O} \quad (19)$$

where \mathbf{O} is a $1 \times n$ zero row vector. Because $\mathbf{C}'^{(\text{exp})} \cdot \mathbf{C}'^{(\text{exp})} = 1.0$, equation (19) becomes

$$\mathbf{C}'^{(\text{exp})} - \left[\frac{\mathbf{S}'_e \mathbf{E}'^{(k-1)}}{|\mathbf{S}'_e \mathbf{E}'^{(k-1)}|} \right]^T \rightarrow \mathbf{O}. \quad (20)$$

Equation (20) can be reduced to

$$\mathbf{C}'^{(\text{exp})} - \frac{\mathbf{S}'_e \mathbf{E}'^{(k-1)}}{|\mathbf{S}'_e \mathbf{E}'^{(k-1)}|} \rightarrow \mathbf{O}. \quad (21)$$

The left-hand side of equation (21) is exactly the same as $\Delta \mathbf{C}'^{(k-1)}$ in the iterative solution in equation (15). Therefore, the iterative solution in equation (15) contains the objective function. Figure 4 shows the iteration process in Cartesian coordinates for the case of $n = 3$. In the iterative process, the sampled vector $\mathbf{C}'^{(k)}$ becomes the experimental vector with experimental capacitance $\mathbf{C}'^{(\text{exp})}$, because the inner product becomes approximately 1.0.

3.4. Convergence condition

Using equation (15), the relationship between the k th iterative solution, $\mathbf{E}'^{(k)}$, and the $(k-1)$ th iterative solution, $\mathbf{E}'^{(k-1)}$, can be rewritten as

$$\mathbf{E}'^{(k)} = \mathbf{S}'_e{}^T \mathbf{C}'^{(\text{exp})} + \left(\mathbf{I}_m - \frac{\mathbf{S}'_e{}^T \mathbf{S}'_e}{|\mathbf{S}'_e \mathbf{E}'^{(k-1)}|} \right) \mathbf{E}'^{(k-1)} \quad (22)$$

where \mathbf{I}_m is a $m \times m$ unit matrix. From this equation, the state transition matrix, \mathbf{T} , between $\mathbf{E}'^{(k)}$ and $\mathbf{E}'^{(k-1)}$ is

$$\mathbf{T} = \mathbf{I}_m - \frac{\mathbf{S}'_e{}^T \mathbf{S}'_e}{|\mathbf{S}'_e \mathbf{E}'^{(k-1)}|} = \mathbf{I}_m - \frac{\mathbf{S}'_e{}^T \mathbf{S}'_e}{|\mathbf{C}'^{(k-1)}|}. \quad (23)$$

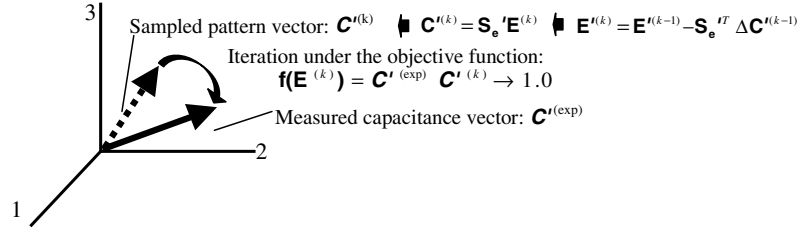


Figure 4. Iteration process of GVSPM in the case of $n = 3$.

Table 1. Differences between Landweber, iterative Tikhonov regularization and GVSPM.

	Normalization of \mathbf{C}	Normalization of \mathbf{S}_e	Empirical value	Objective function for convergence	Convergence at infinite iteration
LW	Every iteration with 0.0 and 1.0	Initial normalization with each row element	α necessary	None	Unknown
ITR	Every iteration with 0.0 and 1.0	Initial normalization with each row element	γ necessary	Minimum least square	Convergence
GVSPM	Every iteration with the norm	Normalization with the norm of the column vector as well as the initial normalization	Unnecessary	Inner product between $\mathbf{C}^{(exp)}$ and $\mathbf{C}^{(k)}$	Convergence

LW: Landweber; ITR: Iterative Tikhonov regularization; GVSPM: Generalized vector sampled pattern matching.

Assuming that $\mathbf{E}^{(k-1)}$ can be represented by the eigenvalue λ of the state transition matrix \mathbf{T} , since $\mathbf{T}\mathbf{E}^{(k-1)} = \lambda\mathbf{E}^{(k-1)}$, this expression can be expanded to

$$\begin{aligned} \mathbf{E}^{(k)} &= \lambda\mathbf{E}^{(k-1)} + \mathbf{E}^{(ini)} = \lambda(\lambda\mathbf{E}^{(k-2)} + \mathbf{E}^{(ini)}) + \mathbf{E}^{(ini)} \\ &= (\lambda^k + \lambda^{k-1} + \dots + \mathbf{I}_m)\mathbf{E}^{(ini)}. \end{aligned} \quad (24)$$

The symmetrical determinant matrix is obtained from the definition of an eigenvalue

$$|\lambda \mathbf{I}_m - \mathbf{T}| = \begin{vmatrix} \lambda & \kappa_{12} & \bullet & \kappa_{1m} \\ \kappa_{12} & \lambda & \bullet & \kappa_{2m} \\ \bullet & \bullet & \bullet & \bullet \\ \kappa_{1m} & \kappa_{2m} & \bullet & \lambda \end{vmatrix} = 0. \quad (25)$$

It is obvious that the modulus of the off-diagonal elements in equation (25) is $|\kappa_{ij}| < 1.0$ because the normalized column vectors of matrix \mathbf{S}_e are less than 1.0. This yields an accurate and stable solution when $k \rightarrow \infty$. Table 1 provides a summary of the differences between the methods based upon the above explanation. The following section explains how these differences influence the solutions.

4. Image reconstruction and discussion

4.1. Image reconstruction conditions

In this section, the Landweber, iterative Tikhonov regularization and GVSPM methods are tested using pseudo particle concentration distribution simulation images of solid–air two-phase flow. The following guidelines are established to compare each method impartially (Zhao *et al* 2002).

- (1) The GVSPM normalized sensitivity matrix is normalized with the norm of the column vector, as detailed in equation (9).

- (2) The first capacitance, which is obtained by multiplying the sensitivity matrix and the original pseudo image, is normalized with a minimum value of 0.0 and a maximum value of 1.0. The first capacitance is the measured capacitance in the real experiments.
- (3) In both the original pseudo images and the final reconstructed images, all the pixels outside the pipe are ignored because the area outside the pipe is not relevant to the image comparisons.
- (4) The capacitances for the LW and ITR methods are normalized with a minimum value of 0.0 and a maximum value of 1.0 after each iteration. The reconstructed image is not normalized by itself.
- (5) The capacitances calculated with the GVSPM method are normalized with the norm after each iteration, as shown in equation (15). The reconstructed image is not normalized by ITR.
- (6) Because the results are normalized by the norm after each iteration, the final images of the GVSPM method provide only relative values. Therefore, the final images and final capacitances must be normalized with a minimum value of 0.0 and a maximum value of 1.0 to calculate C_R , I_E and I_C .
- (7) Not all methods utilize a threshold value at each iteration.
- (8) The reconstructed images with dispersion concentration rates (DCR) are compared with 0% DCR to calculate C_R , I_E and I_C .

Figure 5 shows the simulation images for four types of pseudo particle distributions. Because the actual solid–air two-phase flow image consists of the main particle bulk and dispersion particles around it, 10 different dispersion concentration rates between 0% and 100% are considered. For example, a 10% DCR correlates to a random white noise value between 0.0 and 0.1, which highlights the dispersion particles. These values are assigned to each pixel in the original 0% DCR image. Values

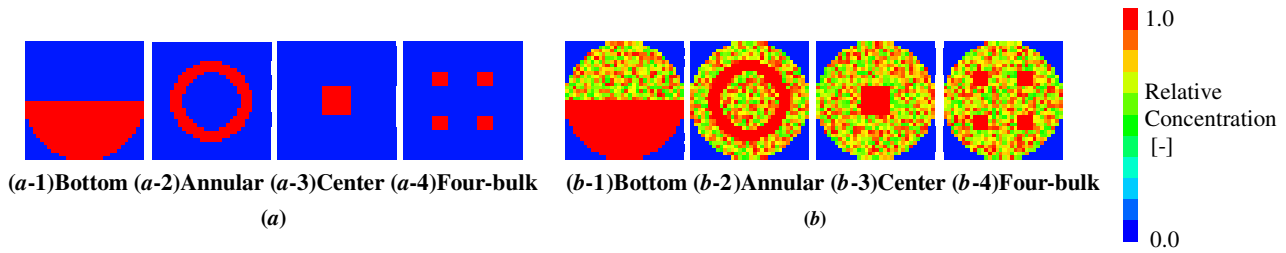


Figure 5. Pseudo particle images. (a) Pseudo particle image with 0% DCR, (b) pseudo particle image with 100% DCR.

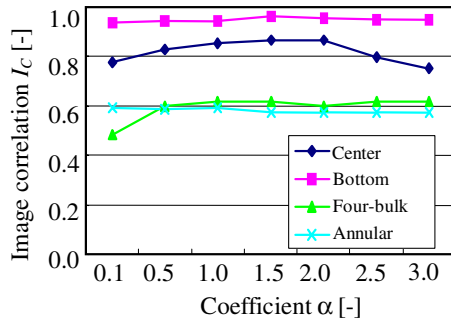


Figure 6. α and I_C in LW in the case of $I = 30$.

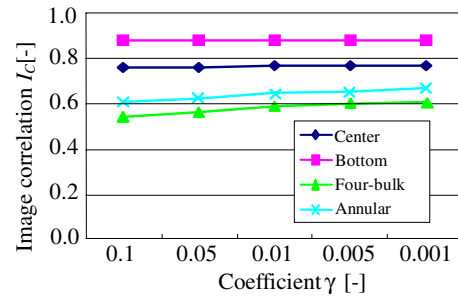


Figure 7. γ and I_C in ITR in the case of $I = 30$.

over 1.0 replace all the pixels with the original pseudo particle images. Figure 5(a) displays the pseudo particle image with a 0% DCR and figure 5(b) shows the representative images for a 100% DCR. In these figures, (*-1), (*-2), (*-3) and (*-4) are the bottom, the annular, the centre and the four-bulk pseudo particles image within the pipe, respectively. In these pseudo images, the red pixels indicate the highest particle concentration, 1.0, and the blue pixels indicate air.

In order to estimate each method quantitatively, the capacitance residual C_R , the image error I_E and the image correlation I_C are calculated using the following:

$$C_R = \frac{\sqrt{\sum_{i=1}^n (c_i^{(k)} - c_i^{(\text{exp})})^2}}{\sqrt{(\mathbf{C}^{(\text{exp})})^2}}$$

$$I_E = \frac{\sqrt{\sum_{i=1}^m (e_i^{(k)} - e_i^{\text{original}})^2}}{\sqrt{(\mathbf{E}^{\text{original}})^2}} \quad (26)$$

$$I_C = \frac{\sum_{i=1}^m [(e_i^{(k)} - \overline{\mathbf{E}^{(k)}})(e_i^{\text{original}} - \overline{\mathbf{E}^{\text{original}}})]}{\sum_{i=1}^m \sqrt{(e_i^{(k)} - \overline{\mathbf{E}^{(k)}})^2} \sum_{i=1}^m \sqrt{(e_i^{\text{original}} - \overline{\mathbf{E}^{\text{original}}})^2}}.$$

In these equations, $e_i^{(k)}$ is the i th element of the final reconstructed image $\mathbf{E}^{(k)}$, $\overline{\mathbf{E}^{(k)}}$ is the special mean pixel value of $\mathbf{E}^{(k)}$, e_i^{original} is the i th element of the original pseudo image $\mathbf{E}^{\text{original}}$, and $c_i^{(k)}$ is the i th element of the final capacitance $\mathbf{C}^{(k)}$ calculated from the final reconstructed image $\mathbf{E}^{(k)}$. The low value of C_R and I_E , the high value of I_C mean accurate reconstructed images.

The LW and ITR methods are highly dependent upon coefficients α and γ to successfully reconstruct the images. These coefficients are fixed in order to compare the reconstructed images. Figure 6 shows the relationship between the LW method's coefficient α and the image correlation

I_C to the four types of 0% DCR image at iteration number $I = 30$ within the 0.1 to 3.0 range. Figure 7 shows the relationship between the ITR method's coefficient γ and the image correlation to the 0% DCR image at $I = 30$ within the 0.001 to 0.1 range. In the case of the centre and bottom images, $\alpha = 1.5$ and 2.0 indicate the relatively high value of I_C , and in the case of the four bulk and annular images, $\alpha > 0.5$ indicate the relatively high value of I_C . Considering the whole situation, the gain α in equation (16) is fixed at 2.0 and the γ in equation (17) is fixed at 0.01 for all the pseudo particle images because of the relatively high correlation value. In order to account for the original differences between various percentage DCR images and the 0% DCR images, C_R , I_E and I_C are calculated before the reconstruction. Figure 8 shows the results of these actions. This figure suggests that C_R and I_E increase, and I_C decreases, as DCR increases for all image patterns.

4.2. Iteration number and reconstructed images

Before the reconstructed images with DCR were compared, the number of iterations and three estimation categories: C_R , I_E and I_C are calculated for the 0% DCR representative image. The simulated measurement capacitance data are noise-free. Figures 9 to 12 show the bottom, the annular, the centre and the four-bulk reconstructed image results for C_R and I_R among the three categories, respectively. The figures I_C are omitted because it is not difficult to guess the value from the later figures in the following section. These figures indicate which methods most strongly depend upon the image type and the iteration number. First, the bottom image in figure 9 reveals that LW is superior to GVSPM and ITR regardless of the number of iterations. Figure 9(a) shows that the value of C_R for the LW method is extremely low, and is approximately the same as for the GVSPM method. Figure 9(b) shows that the value of I_E for LW remains low regardless of the iteration

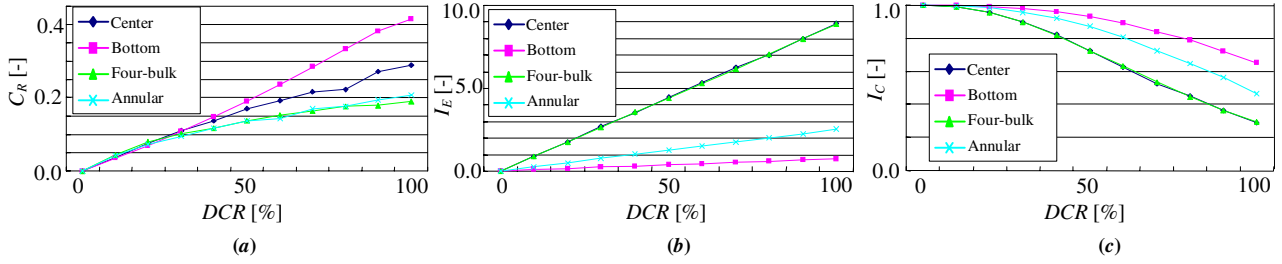


Figure 8. Original differences between various DCR images and 0% DCR image. (a) Capacitance residual, (b) image error, (c) image correlation.

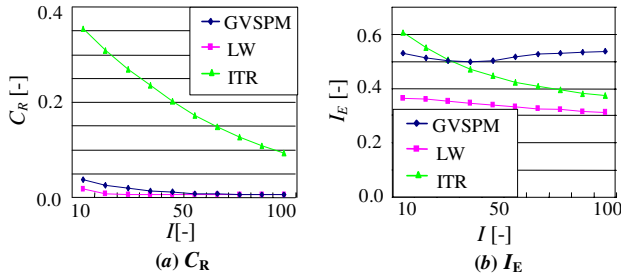


Figure 9. Bottom image.

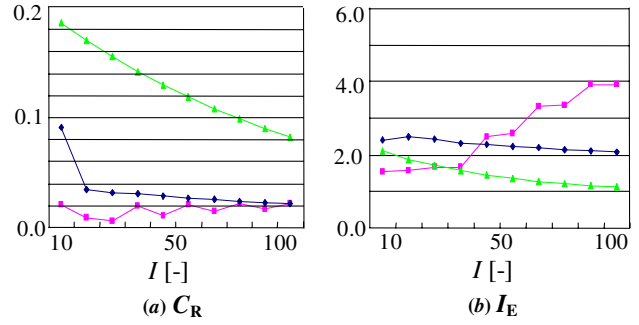


Figure 11. Centre image.

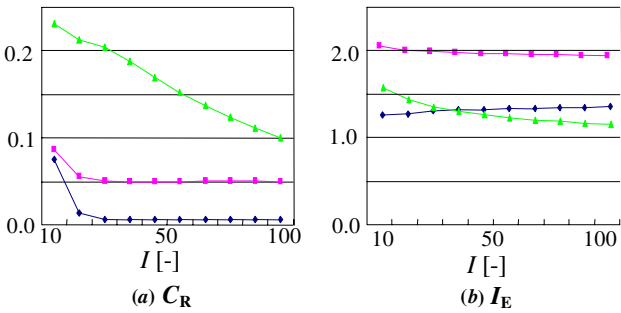


Figure 10. Annular image.

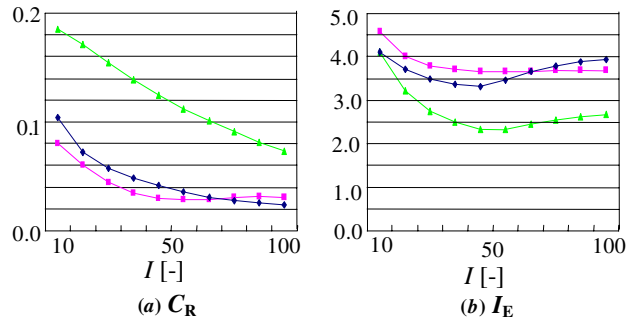


Figure 12. Four-bulk.

number. On the other hand, the I_E values for the ITR method decrease with the iteration number, but never reach the LW level. Finally, the I_C value for the LW method was the highest, when compared with the GVSPM and the ITR methods, and it maintained its high value even after large numbers of iterations.

Secondly, in the case of the annular image shown in figure 10, considering the three estimation categories as a whole, it is determined that the GVSPM method is superior to the LW and ITR methods. Especially, when $I < 30$, the GVSPM method is clearly the best. In figure 10(a), the value of C_R for the GVSPM method is quite low. However, these values for the LW and ITR methods are extremely high. In figure 10(b), I_E for the GVSPM and ITR methods are very low, and when $I < 30$, the values for the GVSPM are much lower than the ITR and LW methods. Moreover, I_C values of the GVSPM and ITR were superior to the LW method. When $I < 40$, though, the I_C values for the GVSPM method were higher than the ITR method.

Thirdly, the superior method in the case of the centre image in figure 11 is strongly dependent upon the iteration number I . As is evident from this figure, the graph patterns are vastly different from the previously mentioned images. Considering the three estimation categories as a whole, it is determined that the LW method is superior to the GVSPM

and ITR methods when $I < 40$. However, when $I > 40$, the GVSPM method becomes superior to ITR and LW. As shown in figure 11(a), the values of C_R for the GVSPM and LW methods are considerably lower than the ITR method, which is extremely high. As shown in figure 11(b) the LW value of I_E is very low under $I = 40$, however, it dramatically increases over $I = 40$. The I_C values for the GVSPM and ITR methods improve until about $I = 100$, when they become saturated. The I_C value for the LW method, though, decreases dramatically as I increases over $I = 60$.

Lastly, the four-bulk reconstructed images displayed in figure 12 are strongly dependent upon I . As a whole, it is very difficult to determine the best method. Figure 12(a) shows that the C_R value for the ITR method is extremely high above $I = 100$. This is a highly negative characteristic. However, figure 12(b) shows that the ITR I_E value is lower than those of GVSPM and LW. The I_C value for ITR was relatively high. These are positive characteristics for this method. The GVSPM and LW methods also have positive and negative characteristics.

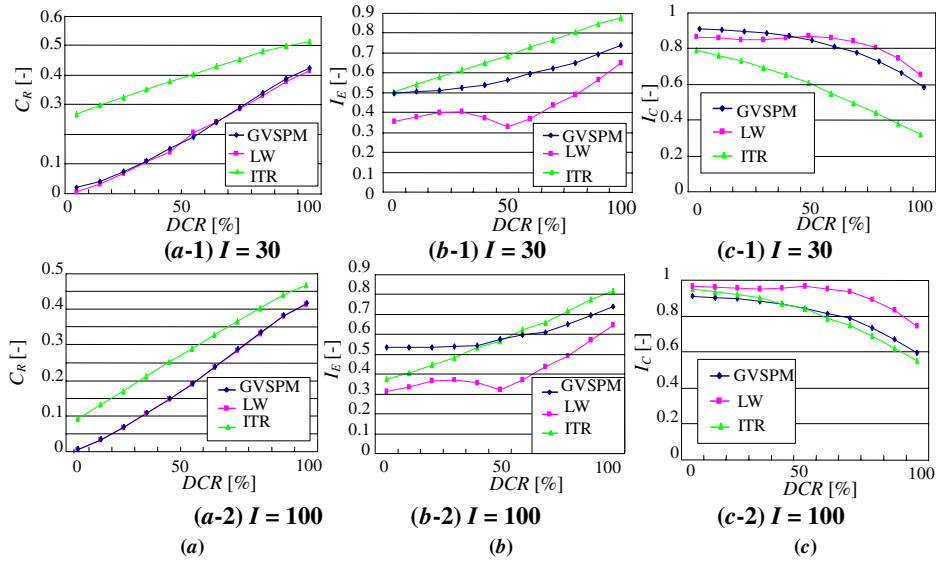


Figure 13. (a) Capacitance residual, (b) image error and (c) image correlation in the case of bottom image.

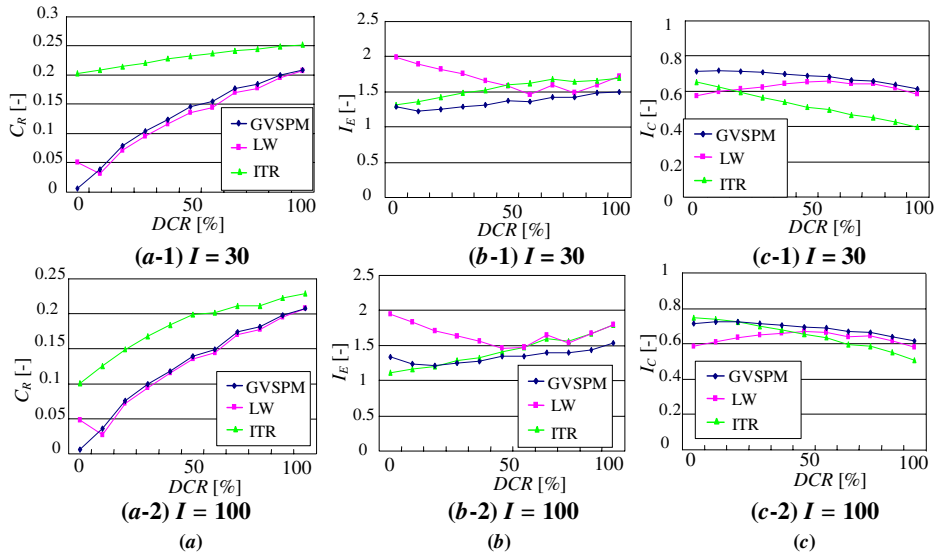


Figure 14. (a) Capacitance residual, (b) image error and (c) image correlation in the case of annular image.

4.3. Comparison among reconstructed images including DCR

Figures 13 to 16 show the estimation categories of the bottom, the annular, the centre and the four-bulk pseudo images including the dispersion concentration rate. In these figures, (a), (b) and (c) show the capacitance residual C_R , the image error I_E and the image correlation I_C , respectively. The (*-1) and (*-2) display the results at iteration numbers $I = 30$ and 100, respectively. In general, C_R and I_E increase and I_C decreases as DCR increases at all I . The superior method is highly dependent upon the image type, the iteration number and DCR. In the case of the bottom image in figure 13, the LW method proves superior to the GVSPM and ITR methods regardless of the iteration number and DCR. Figures 13(a-1) and (a-2) show the C_R value for the LW method is very low and the same as the GVSPM value, however, the C_R value for the ITR method is extremely high. Figures 13(b-1) and (b-2)

display that the I_E value for LW is always the lowest, regardless of I and DCR. Moreover, the I_C value for LW is much higher than for GVSPM and ITR, regardless of I and DCR, as shown in figures 13(c-1) and (c-2).

Next, the annular image in figure 14 is considered. Considering the three estimation categories as a whole, GVSPM is clearly superior to LW and ITR for all DCR values. As shown in (a-1) and (a-2), the value of C_R for the GVSPM and LW methods is lower than C_R for the ITR method. In figure 14(b-1), where $I = 30$, the I_E value for GVSPM is considerably lower than LW and ITR regardless of DCR. As shown in (b-2) in the case of $I = 100$, the I_E values for GVSPM and ITR are lower than LW, specifically, when $DCR > 30\%$, the I_E value for GVSPM is lower than ITR. Moreover, in figure 14(c-1), where $I = 30$, the I_C value for GVSPM is higher than those of LW and ITR regardless of DCR. When DCR surpasses 30%, though, as in figures 14(c-2) $I = 100$, the I_C value for the GVSPM is higher than those of LW and ITR.

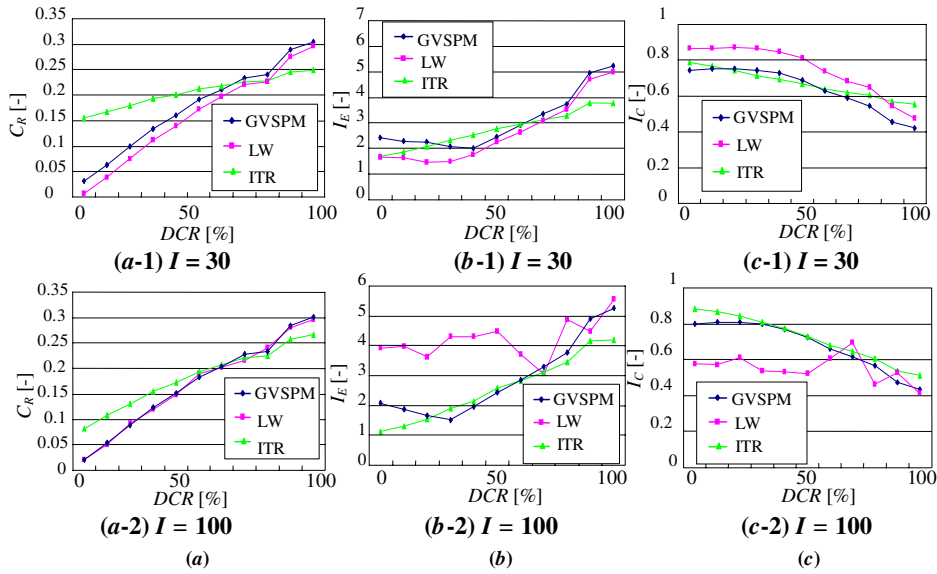


Figure 15. (a) Capacitance residual, (b) image error and (c) image correlation in the case of centre image.

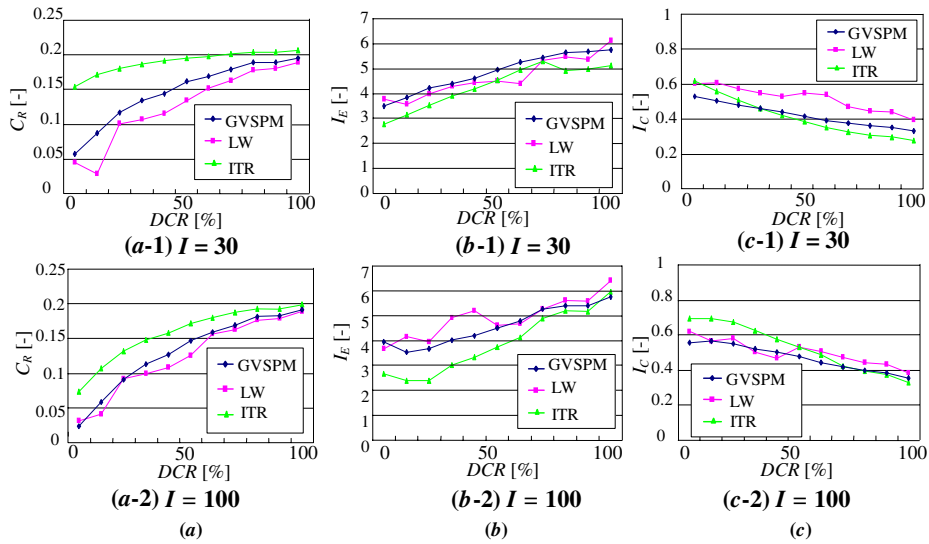


Figure 16. (a) Capacitance residual, (b) image error and (c) image correlation in the case of four-bulk image.

The reconstructed images in the case of the centre image of figure 15 are highly dependent on I and DCR. It is known from the results in section 4.2 that when $I < 40$ and $DCR < 80\%$, LW is superior to GVSPM and ITR. And when $I < 40$ and $DCR > 80\%$, ITR is superior to GVSPM and LW. However, when $I > 40$, considering C_R , I_E and I_C as a whole, GVSPM and LW become superior to ITR. More specifically, in the case in figure 15(a-1), where $I = 30$, the values of C_R under $DCR = 80\%$ for the GVSPM and LW methods are smaller than those of ITR. In the case of (a-2) $I = 100$, these differences in C_R become very small across all three methods. Figure 15(b) shows that the I_E values for the (b-1) $I = 30$ case become almost the same for all three methods. However, as the number of iterations increases, as in (b-2) $I = 100$, the I_E values for GVSPM and ITR improve and decrease below that of LW. Here, the GVSPM I_E values are almost the same as those for ITR for all DCR. The results from figure 15(c)

indicate that the I_C correlation values for LW are higher than those of GVSPM and ITR in the case of (c-1) $I = 30$ and $DCR < 80\%$. However, in the case (c-2) $I = 100$, the GVSPM and ITR correlation values become superior to LW, whose I_C value becomes extremely low.

Finally, the four-bulk reconstructed images shown in figure 16 are strongly dependent on I and DCR. It is difficult to determine the best method. When $I < 30$, the value of C_R for the LW is clearly superior to those of GVSPM and ITR for all DCR as shown in (a-1). However, these differences diminish as I increases, as shown in (a-2). Figure 16(b) displays the results for I_E . In the (b-1) $I = 30$ case, the ITR value is lower than the LW and GVSPM cases except for $DCR = 60\%$. As shown in (b-2), the I_E value for the ITR becomes lower than those of LW and GVSPM. Moreover, the I_E value for LW becomes unstable against DCR in the (b-2) $I = 100$ case. And although the I_C value for LW is higher than that for GVSPM

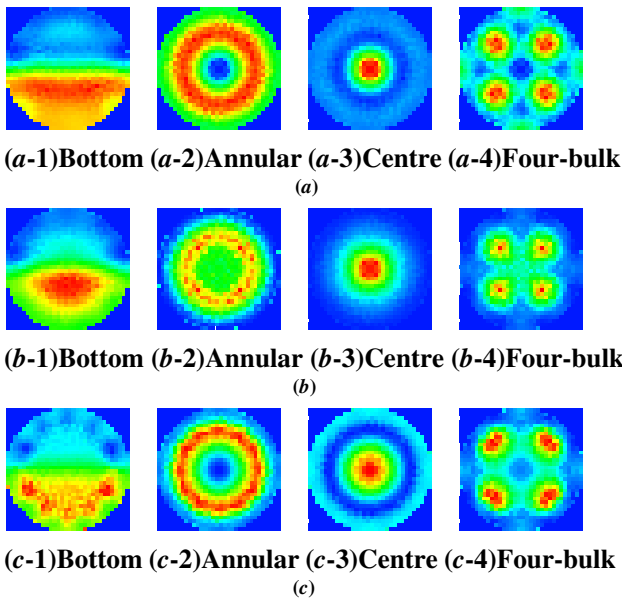


Figure 17. Reconstructed images of 0% DCR. (a) Reconstructed image by Landweber, (b) reconstructed image by iterative Tikhonov and (c) reconstructed image by GVSPM.

Table 2. Best method for image types.

Image type	Best reconstruction method
Bottom image	LW
Annular image	GVSPM
Centre image	
$I < 40$	DCR < 80% LW DCR > 80% ITR
$I > 40$	GVSPM or LW
Four-bulk image	Difficult to judge

GVSPM: generalized vector sampled pattern matching; ITR: iterative Tikhonov regularization; LW: Landweber.

and ITR in figure 16(c-1) $I = 30$, GVSPM and ITR's I_C values become superior to LW as I increases, as is evident in (c-2), however, LW is not stable against DCR. The details for each method are summarized in table 2 below. It is clear which method is the best for the images. According to figures 13 through 15, the category difference between $I = 30$ and $I = 100$ of GVSPM is not so large as compared with that of LW or ITR. This is a strong point of GVSPM, which LW or ITR does not have.

The representative reconstructed images that were obtained using each method are presented in figures 17 and 18 as a reference. Figure 17 shows the images for $I = 30$ and 0% DCR, and figure 18 shows the results for $I = 30$ and 100% DCR. From these figures it is evident that the annular images reconstructed using the GVSPM method are very clear, but the centre images reconstructed using GVSPM are blurred. According to figure 17, GVSPM has a tendency of artefact when the particle concentration is partial in the case such as the bottom image. However, a uniform particle concentration image such as annular image in the cross section does not produce the artefact. It is confirmed that the $\mathbf{f}(\mathbf{E}^{(k)})$ value converges to 1.0 and then becomes saturated over $I = 30$ in

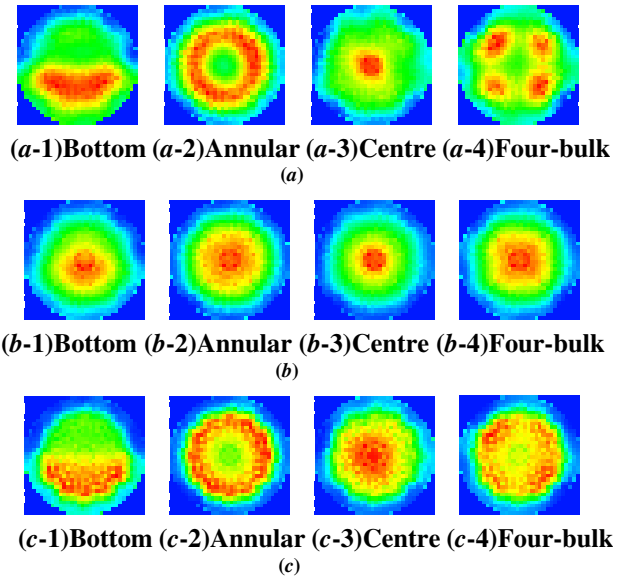


Figure 18. Reconstructed images of 100% DCR. (a) Reconstructed image by Landweber, (b) reconstructed image by iterative Tikhonov and (c) reconstructed image by GVSPM.

all conditions. This highly accurate reconstruction does not use an empirical value because the GVSPM method contains an objective function that makes the inner product between $\mathbf{C}^{(\text{exp})}$ and $\mathbf{C}^{(k)}$ in equation (6) become 1.0 ($\Delta \mathbf{C}^{(k-1)} \rightarrow \mathbf{0}$ in equation (15)). However, because the LW does not utilize an objective function and ITR has only a minimum least square criterion, matching between the experimental capacitance and the reconstructed image capacitance is not compensated during the iteration process.

5. Conclusions

The generalized vector pattern matching method has been applied to an ill-posed inverse problem involving the electrical capacitance for solid–air two-phase flow. Four types of pseudo particle distribution images with dispersion concentration rates were used to compare the GVSPM method to the conventional Landweber and iterative Tikhonov regularization methods. The results of these comparisons are detailed below:

- (1) GVSPM is superior to the LW and ITR methods for annular pseudo particle images in terms of capacitance residual, image error and image correlation, even though the GVSPM method does not use an empirical value. The GVSPM iteration process also proved to be very stable.
- (2) In the case of the bottom pseudo particle, the LW method outperformed the GVSPM and ITR methods.
- (3) For the centre image and four-bulk image cases, the superior method depends on the iteration number and the DCR. For example, in the case of the centre image, when $I < 40$ and DCR < 80%, the LW proved superior to the GVSPM and ITR methods. When $I < 40$ and DCR > 80%, the ITR proved superior to the GVSPM and LW methods. However, when $I > 40$, the GVSPM and LW methods outperformed the ITR method. In the case of the four-bulk image, it is difficult to determine the best method.

Acknowledgments

The authors would like to thank Professor Tomsz Dyakowski of UMIST and Professor Richard Williams of Leeds University in the UK for providing useful advice.

References

- Dyakowski T, Luke S P, Ostrowski K L and Williams R A 1999 On-line monitoring of dense phase flow using real-time dielectric imaging *Powder Technol.* **104** 287–95
- Endo H, Hayano S, Saito Y and Miya K 2002 Generalized vector sampled pattern matching method—theory and applications *Electromagnetic Nondestructive Evaluation (VI) (Studies in Applied Electromagnetics and Mechanics vol 23)* ed F Kojima (Netherlands: IOS Press) pp 285–92
- Halow J S and Nicoletti P 1992 Observations of fluidized bed coalescence using capacitance imaging *Powder Technol.* **69** 255–77
- Huang S M, Plaskowski A B, Xie C G and Beck M S 1989 Tomographic imaging of two-component flow using capacitance sensors *J. Phys. E: Sci. Instrum.* **22** 173–77
- Isaksen O 1996 A review of reconstruction techniques for capacitance tomography *Meas. Sci. Technol.* **7** 325–37
- Liu S, Fu L and Yang W Q 2001 Comparison of three image reconstruction algorithms for electrical capacitance tomography *Proc. 2nd World Congress on Industrial Process Tomography (Hanover, Germany)* pp 29–34
- Polydorides N and Lionheart W R B 2002 A Matlab toolkit for three-dimensional electrical impedance tomography: a contribution to the Electrical Impedance and Diffuse Optical Reconstruction Software project *Meas. Sci. Technol.* **13** 1871–83
- Saito Y, Itagaki E and Hayano S 1990 A formulation of the inverse problems in magnetostatic fields and its application to a source position searching of the human eye fields *J. Appl. Phys.* **67** 5830–2
- Saotome J, Coulomb J L, Saito Y and Sabonnadiere J C 1995 Magnetic core shape design by the sampled pattern matching method *IEEE Trans. Magn.* **31** 1976–9
- Williams R A and Beck M S 1995 *Process Tomography Principles, Techniques and Applications* (Burlington, MA: Butterworth-Heinemann) chapter 15, pp 301–12
- Yang W Q 1996 Hardware design of electrical capacitance tomography systems *Meas. Sci. Technol.* **7** 225–32
- Yang W Q and Peng L 2003 Image reconstruction algorithms for electrical capacitance tomography *Meas. Sci. Technol.* **14** R1–13
- Yoda K, Saito Y and Sakamoto H 1997 Dose optimization of proton and heavy ion therapy using generalized sampled pattern matching *Phys. Med. Biol.* **42** 2411–20
- Zhao J, Fu W, Li T and Wang S 2002 An image reconstruction algorithm based on a revised regularization method for electrical capacitance tomography *Meas. Sci. Technol.* **13** 638–40